Electronic Structure and Growth of Electrochemically Formed Iridium Oxide Films

Liudmila Ilyukhina,[a] Svein Sunde,[a,*,z] and Richard G. Haverkamp ![ORCID][b]

*[a]Department of Materials Science and Engineering, Norwegian University of Science and Technology (NTNU),
NO-7491 Trondheim, Norway*
[b]School of Engineering and Advanced Technology, Massey University, Palmerston North, New Zealand
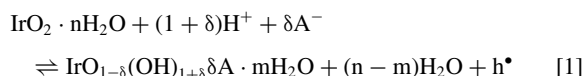
The nature of the electronic structure of electrochemically formed iridium oxide films (EIROF) is investigated by in-situ conductivity measurements in an electrochemical cell and ex-situ current-sensing atomic force microscopy (CS-AFM). A direct demonstration of changes in the conductivity for electrochemically formed iridium oxide films (EIROF) with the applied potential of EIROF electrodes in an electrochemical cell is presented. The in-situ conductivity shows a single step-like change at a potential of approximately 1.2 V in 0.5 mol dm^{-3} H$_2$SO$_4$ vs. a reversible hydrogen reference electrode. The change in conductivity is also reflected in results of ex-situ CS-AFM for EIROF electrodes emersed at different potentials. At an emersion potential of 0 V the CS-AFM current-voltage characteristics are non-linear and similar to those of diodes. At an emersion potential of 1.6 V the CS-AFM current-voltage characteristics are approximately linear, consistent with metallic behavior. Mott-Schottky analysis shows that at low potentials the oxide behaves as a p-type semiconductor with a flatband potential approximately 500 mV below the transition to high conductivity from the in-situ conductivity measurements. These results allow for an interpretation of changes in the relative magnitudes of the III/IV and IV/V (or IV/VI) voltammetric peaks during film growth through a block-release behavior involving space-charge layers in the oxide.

Iridium oxide[1] is relevant as a material for electrochromics,[2–4] electrocatalysis[5–19] and as a pH sensor.[20] A proposed mechanism for the electrochromic properties of the material based on the electronic structure was suggested by Granqvist.[3,4] According to this explanation the change of color with potential is due to variations in band filling associated with intercalation of protons and possibly other ions,[21]

$$IrO_2 \cdot nH_2O + (1 + \delta)H^+ + \delta A^-$$

$$\rightleftharpoons IrO_{1-\delta}(OH)_{1+\delta}\delta A \cdot mH_2O + (n - m)H_2O + h^\bullet \quad [1]$$

where A$^-$ is a solution anion, and h$^\bullet$ and electron hole.

For oxygen-evolution electrocatalysts one expects the activity to depend on the binding energy of intermediates involved in the reaction according to the Sabatier principle. Since the binding energy of the various relevant intermediates appear to scale with the binding energy of oxygen, the latter quantity may serve as a descriptor of catalytic activity for the oxygen evolution reaction. Exactly how the features of the electronic structure of the catalyst are related to the binding energy appears to be less clear than in the case of metals for which the d-band theory and its refinements[22,23] appear to successfully rationalize electronic structure and (electro-) catalytic behavior. Recent work indicates that the number of electrons in the d-band of transition metal oxides is an important descriptor of catalytic activity,[24,25] although other aspects of the electronic structure may be important as well.[26]

Also other electrochemical properties such as the shapes of voltammograms have been attempted analyzed in terms of electronic structure.[27]

It is therefore of interest to characterize properties reflecting the electronic structure of the various forms of iridium oxide, preferably in-situ, to rationalize the various aspects of the oxide on common platform. The band structure of iridium oxide[28–30] suggests that one should expect the oxide to switch its conductivity from low to high upon oxidation. Measurements of changes in the conductivity of the oxide during the process therefore appear particularly important. Indirect or ex-situ evidence of such switching is available for anodically formed iridium oxide films (AIROF) in the literature,[31,32] but direct evidence is scant. Kukkonen et al.[33] measured the resistance of iridium electrodes during passivation by measuring the resistance between two identical electrodes contacting one another, face to face. These

results do not comply with those expected from the band structure of the oxide, however, and it is thus not quite clear how they relate to the electronic structure of the oxide being formed.

Also, various forms of iridium oxide exist, and these may display significant differences in their properties. Thus anodically formed iridium oxide films (AIROFs) display distinct semiconducting behavior in the reduced form and metallic properties in the oxidized form.[32] A similar transition was not observed for iridium oxide synthesized by hydrolysis.[17] Electrochemically formed iridium oxide films (EIROFs)[34,35] are particularly interesting forms of iridium oxide from the perspective of making thin iridium oxide layers for high utilization of iridium. Their electronic properties are therefore correspondingly relevant.

In this work we directly document changes in conductivity of electrochemically formed iridium oxide films (EIROF) with the use of an in-situ conductivity probe.[36–38] We also include ex-situ measurements of surface conductivity by current-sensing atomic force microscope (CS-AFM) and show that these are consistent with the direct assessment. Finally, we demonstrate how these measurements can be used to analyze the growth mechanism and electrochemical properties of EIROF in terms of the electronic structure.

Experimental

Electrodes.—Glassy carbon and gold electrodes were used as substrates for the electrodeposited iridium oxide layers. The electrodes were embedded in epoxy together with electrical contacts at the back side of the electrode. After casting, the embedded electrodes were polished until mirror finish (to 1 μm for carbon and 0.05 μm for the softer gold electrodes) so that the electrode surface was flush with the insulating epoxy surrounding it. The polished electrodes were rinsed with water and washed twice for 10 min in an ultrasonic bath. The geometric area for the glassy carbon electrode employed in this paper was approximately 1 cm². The polished gold electrodes appeared to be too rough for characterization in the current-sensing atomic force microscope (CS-AFM, see below) and were used mainly for in-situ conductivity measurements as well as in the initial phases to adjust the deposition process. Thus, for CS-AFM all electrode substrates employed were glassy carbon.

Electrodeposition of iridium oxide.—Precursor solutions for electrodeposition were prepared in a similar way to that described in

---

*Electrochemical Society Member.
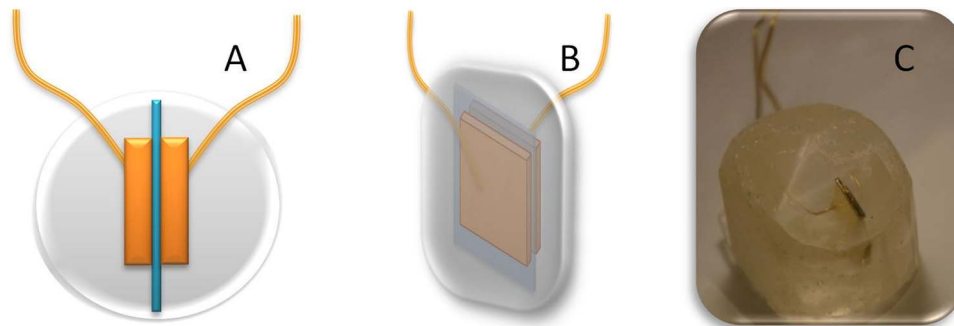zE-mail: Svein.Sunde@material.ntnu.no

Figure 1. Probe for in-situ conductivity measuremets. A: Top view. B: Perspective. C: Photo of the actual cell.

Ref. 35. Thus, an aliquot of H_2IrCl_6 solution was added to 50 ml of water (deionised, 18 MΩ), and stirred for 30 min. Aqueous H_2O_2 (0.5 ml, 30%, Alfa Aesar) was added, and the resulting solution was stirred for 10 min. Potassium oxalate (460 mg Alfa Aesar) was added and the solution was stirred for another 10 min. The pH was slowly adjusted to 10.5 by the addition of potassium carbonate (Aldrich). The resulting yellowish brown solution was covered and heated carefully to 60°C and kept at this temperature for 1 h, after which it appeared deep purple. The prepared solutions were in some cases stored in a fridge at +4°C for up to four weeks. In case the solution appeared darker due to formation of suspended particles during the precursor synthesis or after storage the electrochemical synthesis was no longer reproducible. These solutions were discarded. Also, after electrodepositing large amounts of IrO_x from the same solution further electrodeposition was found to be less reproducible than desirable. This was due to the iridium precursor concentration in the solution dropping to too small values. At this point these solutions were also discarded.

The deposition of IrO_x was carried out in a conventional three-electrode cell by cyclic voltammetry at 100 mV s^{-1} with a Zahner electrochemical workstation (potentiostat) IM6eX and a 3 mol dm^{-3} Ag/AgCl reference electrode. The counter electrode was a Pt mesh. The combination of potential range and substrate was decisive for the characteristics of the resulting iridium oxide layer. At gold substrates a potential range of −0.6 V through 0.8 V vs. Ag/AgCl resulted in a film contained within the electrode substrate itself. A potential range of −0.6 V through 0.95 V, however, resulted in iridium oxide layers extending beyond the gold surface and onto the epoxy.[39] As the in-situ conductivity measurements assumes that the gap between the two edges constituting the probe is bridged by iridium oxide, we consequently always employed the potential range −0.6 V through 0.95 V for this type of electrode. At carbon electrodes the potential range was −0.6 V through 1 V. The number of cycles was varied according to the targeted film thickness, as is discussed in each case presented below.

Note that the method above represents a slight modification of the procedure in Ref. 35. According to recommendations given in Ref. 34 the oxalic acid originally used in Ref. 35 was replaced by potassium oxalate, and additional heating was applied to develop the color of the solution more quickly. Also, H_2IrCl_6 was used instead of anhydrous $IrCl_4$, the amount of H_2IrCl_6 being adjusted to give the same total amount of iridium as in 70 mg of anhydrous $IrCl_4$.[35] This was done based on the mass of iridium (as reported by the supplier) per 1 ml solution.

Electrochemical characterization.—Electrochemical characterization consisted of cyclic voltammetry and measurements of capacitance. After deposition the electrodes were rinsed by leaving them for 10 min in at least three different phosphate buffer solutions (0.1 mol dm^{-3} Na_2HPO_4 and 0.1 mol dm^{-3} KH_2PO_4) in order to remove precursor solution from the film. They were then transferred while wet into an electrochemical (glass) cell filled with a phosphate buffer solution of the same concentration, with a Pt mesh counter electrode and a reversible hydrogen reference electrode (RHE). The cell was flushed with argon prior to the experiments. An argon atmosphere was maintained above the solution at all times during the experiments. The film was cycled at 150 mV s^{-1} until the cyclic voltammograms were stable. Capacitance data for Mott-Schottky plots were collected at 1 kHz in 0.5 mol dm^{-3} H_2SO_4.

In-situ conductivity measurements.—For in-situ conductivity measurements a design similar to that presented in Ref. 36 was employed and is illustrated in Fig. 1. Two epoxy-embedded gold electrodes (prepared as above and with gold plates of 1 mm thickness) were sandwiched face to face but with a thin poly-ethylene (PET) foil in between them. This sandwhich configuration ensures the absence of any direct electrical contact between the two gold plates. The whole sandwich was fixed together by conventional office Scotch 3M^{TM}tape and placed into a mold with a fast-curing epoxy. After hardening, the epoxy bulb with the embedded electrodes was cut across so that two parallel gold edges were exposed at the surface. The electrode was polished as described above in the direction along the PET film. (If polished across, the two gold edges tended to make electrical contact with one another due to polishing damage.) The absence of electrical contact between the gold plates was verified by a multimeter. The resulting exposed geometric area of one gold edge electrode was approximately 4 mm^2.

In-situ conductivity measurements employed a similar circuitry as that in Ref. 36 Thus, the working-electrode connection of a Wenking MP04 minipotentiostat was connected to one of the two gold plates of the in-situ conductivity probe (see above). We will refer to the gold plate to which the working electrode connection of the minipotentiostat was connected as the leading electrode. The counter-electrode and reference-connections of the minipotentiostat were connected to the counter electrode and reference electrode, respectively, as in a standard electrochemical cell. The potential of the leading electrode was thus controlled by the minipotentiostat with respect to the RHE reference electrode in the cell. (The ground link was removed from the minipotentiostat prior to the experiments.) The leading electrode was also connected to the working and sense electrode connections of a Zahner IM6eX potentiostat. The other gold plate of the in-situ conductivity probe was connected to both the reference and counter electrode connections of the Zahner potentiostat. The Zahner potentiostat was thus employed in a two-electrode mode across the gap between the two gold plates. A steady 20 mV potential was imposed across the two gold plates of the conductivity probe by the Zahner potentiostat. The resistance across the film was measured using the built-in functionality of the Zahner potentiostat for measuring ohmic resistance. The resistance of the film was thus measured as a function of the potential of the leading electrode with respect to the RHE reference electrode as controlled by the minipotentiostat. The in-situ conductivity measurements were performed in 0.5 mol dm^{-3} H_2SO_4.

For all the leading-electrode potentials at which the conductivity was measured, we also measured the conductivity of the film immediately after disconnection of the minipotentiostat, i. e. at unrelaxed OCP. This resulted in slightly different values for the

conductivity. However, the results were parallel as a function of the leading-electrode potential, and we will not report the results for the conductivity measurements performed at OCP.

Current-sensing atomic force microscopy.—The CS-AFM measurements were performed with an Agilent Series 5500 AFM/STM instrument and a 100 μm range N9524 scanner. The scanner was equipped with an N9541A CS-AFM nose cone with a nose cone preamplifier of current range 10 nA. Gold-covered silicon current sensing tips were employed in all experiments.

The electrodes for CS-AFM were prepared in the following manner. After electrochemical characterization in phosphate buffer as described in Electrochemical characterization section above the carbon-supported working electrodes were charged either at 0 V or 1.6 V (as specified for each electrode below) for at least 1 min in the electrochemical cell employed for the electrochemical characterization. The crocodile clip contacting the electrode was then disconnected while the potential was still being applied and while the electrode was still in the solution. The electrode was then removed immediately from the solution and rinsed gently with deionized water to remove electrolyte from the film surface. (It is important that the water stream is not directed directly at the deposited layer. In cases where it was, flakes of electrode material were coming off the electrode. These electrodes were discarded.) Excess water at the film surface was collected by contacting lint-free tissue with the rim of the electrodeposited layer, leaving the film surface itself untouched. The entire operation, from disconnecting the potential through rinsing to excess water removal, was always carried out in less than 1 min. This is important because separate experiments showed that the open circuit potential (OCP) after charging at 1.6 V would relax at times longer 1 min to a final, stable potential of approximately 0.8 V. The relaxation from 0 V to higher potentials occurred more slowly, but also for these electrodes the disconnection of the potential and removal of the electrolyte solution was performed in less than 1 min. The electrode was then left to dry overnight in air, after which the dried electrodes were mounted in the microscope for study.

Results

Electrochemical deposition.—Cyclic voltammograms for 100 cycles of EIROF film growth on a glassy carbon electrode are presented in Fig. 2. The figure shows every 10th cycle in the growth process. During the first 50 cycles the CVs resemble previous published results on iridium oxide film growth[35] and a steady increase in the current with increasing number of cycles is apparent. A sudden change in the CVs is observed after approximately 50 cycles, however; the peak at around 0 V ("A-peak" in the figure) decreases considerably between 50 and 70 cycles, while the peak current of the peak at 400 mV ("B-peak" in the figure) continues to increase. For the latter a significant anodic shift in the peak potential is also apparent, however. Between 70 and 100 cycles the A-peak increases again, while the B-peak gets broader without much increase in peak current. The peak currents for the two peaks are shown in the inset of Fig. 2 as function of cycle number, which shows the peak development as described above. Note the simultaneous change in the two peak currents. This effect was also observed when depositing EIROF at gold-supported electrodes. The appearance of the voltammograms in Fig. 2 are very different from those for iridium metal growth presented by El-Sawy and Birss,[40] and indicate the direct formation of the oxide.

In order to simplify the discussion below, we now classify the EIROF films into three different types. We will refer to films grown with a number of cycles fewer than that causing the drop in the A-peak current in the inset of Fig. 2 as type-I films. Films grown with a number of cycles larger than the number of cycles required for the peak current of the A-peak first to decrease and then to increase again will be referred to as type-III films. Films grown with a number of cycles in between those corresponding to type-I and type-III will be referred to as type-II films. Obviously, since the charge of type-I films is less than those of type-II films, in turn smaller than that of type-III
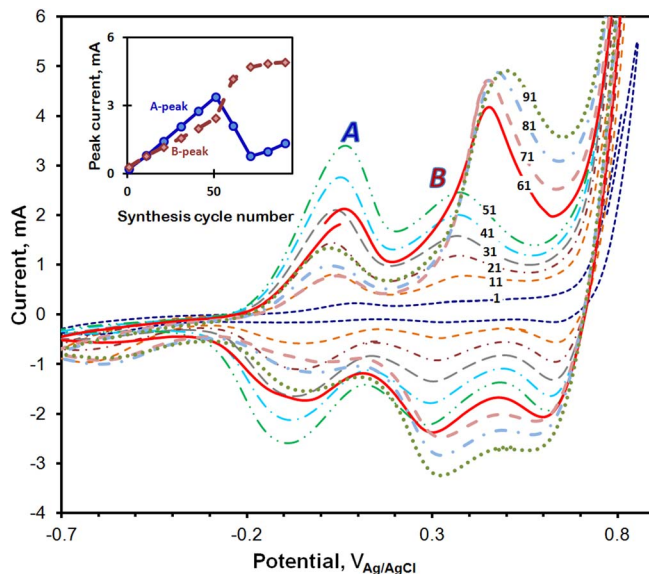

Figure 2. Cyclic voltammograms collected during growth of EIROF on the glassy carbon electrode in a solution containing H_2IrCl_6, H_2O_2, NaC_2O_4, and $NaCO_3$ (see Electrodeposition of iridium oxide section for details). The inset shows peak currents as a function of cycle number. Blue: peak at 0 V. Pink: peak at 400 mV. The potentials are stated vs. the Ag/AgCl reference electrode.

films, type-I would in some sense be thinner than type-II or type-III films. Note that the cycle number representing the transition between the different film types depended also on the anodic potential limit and the sweep rate during synthesis.

Electrochemical characterization and in-situ conductivity measurements.—A set of cyclic voltammograms in phosphate buffer for two EIROF films, recorded at a number of different scan rates, are shown in Figures 3 and 4. The CVs in Fig. 3 were recorded for a type-I film, that in Fig. 4 for a type-III film. Both films were grown for 100 cycles, but the anodic potential limit for the Type-I film was 740 mV (Fig. 3). For the type-III film (Fig. 4) the anodic potential limit was 860 mV vs. Ag/AgCl. The sweep rate was the same as that used in Fig. 2 in both cases (100 mV/s). The voltammograms for
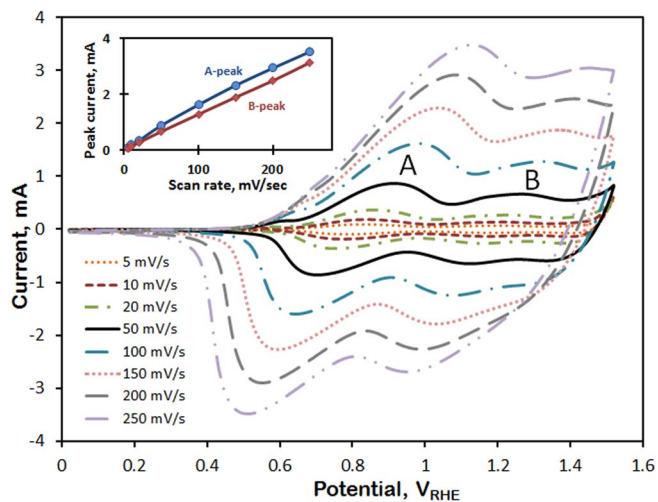

Figure 3. Cyclic voltammograms and peak current vs. scan rate (inset) recorded in phosphate buffer solutions (0.1 mol dm^{-3} Na$_2$HPO$_4$ and 0.1 mol dm^{-3} KH$_2$PO$_4$) for carbon supported sample type I. The A peak corresponds to the peak at approximately 0 V vs Ag/AgCl and B to the peak at approximately 0.4 V vs. Ag/AgCl in Fig. 2.

Figure 4. Cyclic voltammograms and inset with peak current vs. sweep rate in phosphate buffer solutions (0.1 mol dm^{-3} Na$_2$HPO$_4$ and 0.1 mol dm^{-3} KH$_2$PO$_4$) for carbon-supported an EIROF sample of type III. The A peak corresponds to the peak at approximately 0 V vs Ag/AgCl and B to the peak at approximately 0.4 V vs. Ag/AgCl in Fig. 2.
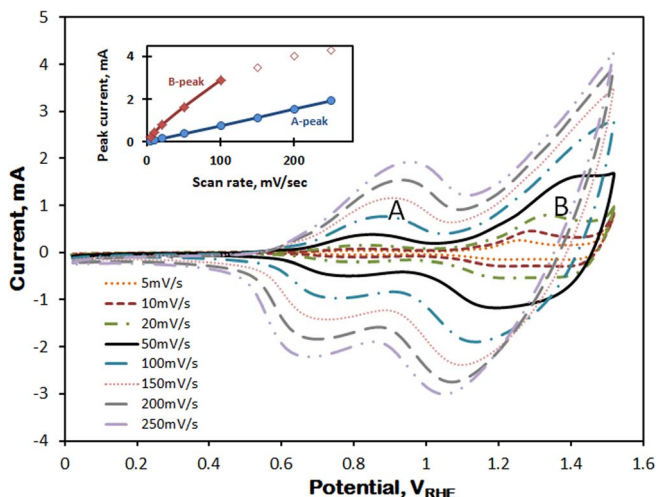
the type-I films in Fig. 3 are qualitatively similar to CVs previously reported by a number of groups, for example for AIROF and EIROF films.[1,18,21,35,41-44] The CVs of the type-III film in Fig. 4 also have their counterparts in the literature,[45] but these shapes appear to be less common.

The peak potentials vs sweep rate are shown for both films in the insets of Figures 3 and 4. The peak current for the A-peak of the type-I film is almost linearly dependent on the sweep rate for small sweep rates in Fig. 3, and roughly so at larger sweep rates. For the same type-I film, B-peak currents are close to perfectly linearly dependent on the sweep rate. The values for peak currents are in the same range for A- and B- peak. For the Type-III film in Fig. 4 the peak current for the A-peak appears to be linear in scan rate, while B-peak currents are not. For the last three points the B-peak did not reach its maximum due to the peak being shifted with sweep rate to potentials higher than the anodic limit of the CVs. For type-III film the peak currents for the

B-peak are much larger than those for the A-peak, and the average slope is also larger.

Type-I EIROF films on gold were observed to be electrochromic, displaying a dark blue color at high (anodic) potentials and being transparent at low (cathodic) potentials. Thicker films had a black appearance not varying with potential. However, type-III films were not always completely uniform, and fringe areas were in some cases observed to display electrochromism also for these films. On glassy carbon it was difficult to see any color change due to the black support.

Mott-Schottky plots from capacitance data collected for these electrodes are shown in Fig. 5. The intercept of the negatively sloping (approximately straight) line for $1/C^2$ (C being the measured capacitance) with the potential axis indicate a flatband potential of approximately 0.65 V vs. the reversible hydrogen reference electrode in phosphate buffer (pH=6.9). Fig. 5 also shows the conductivity of an EIROF sample deposited on the double gold conductivity probe vs. potential of the leading electrode as described in the Experimental section. For reference a 5 mVs^{-1} cyclic voltammogram of the synthesized EIROF in the same solution and same reference electrode is also given in the figure.

From Fig. 5 the conductivity is observed to be low and constant at potentials below the redox peak at 1250 mV vs. RHE (the B-peak). An almost step-wise increase in conductivity is present at 1.2 V, and the conductivity remained high and approximately constant at potentials above 1350 mV, even during formation of oxygen bubbles in the OER region. The "anodic conductivity", i. e. the conductivity above the B-peak (1250 mV), is thus significantly higher than the "cathodic conductivity", the conductivity below the B-peak (1250 mV). The flatband potential has a value well below that at which the transition to the high anodic conductivity occurs, however. The transition appears at approximately the same potential relative to the voltammogram as that observed by Silva et al.,[41] i.e. around the onset of the first peak in the voltammogram.

As opposed to measurements performed dynamically, for example those on poly-3-methylthiophene by Sunde et al.,[36] our conductivity measurements displayed no hysteresis on returning to low potentials since the measurements here were performed in a quasi-steady state.

CS-AFM.—A summary of results for type-I film electrodes on carbon emersed at 0 V and at 1.6 V are presented in Figs. 6 and 7. The figure shows two sets of data; the set in Fig. 6 is for the sample emersed at an applied potential of 0 V, and the set in Fig. 7 is for the sample emersed at 1.6 V (see Experimental). For each set a
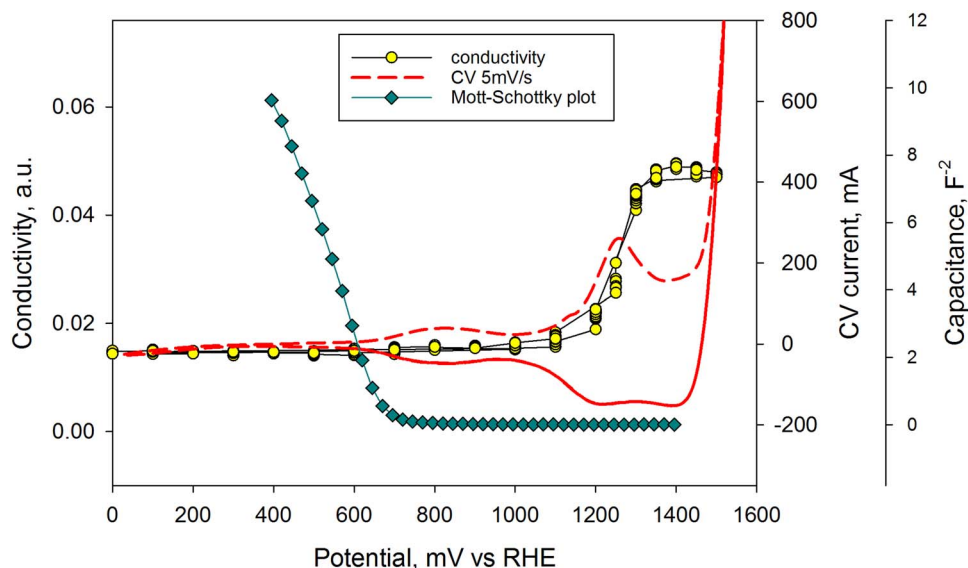

Figure 5. Conductivity under potential control collected for an EIROF on gold substrate in 0.5 mol dm^{-3} H$_2$SO$_4$. The figure includes a Mott-Schottky plot and a voltammogram for a film on carbon support collected at a sweep rate of 5 mVs^{-1}.
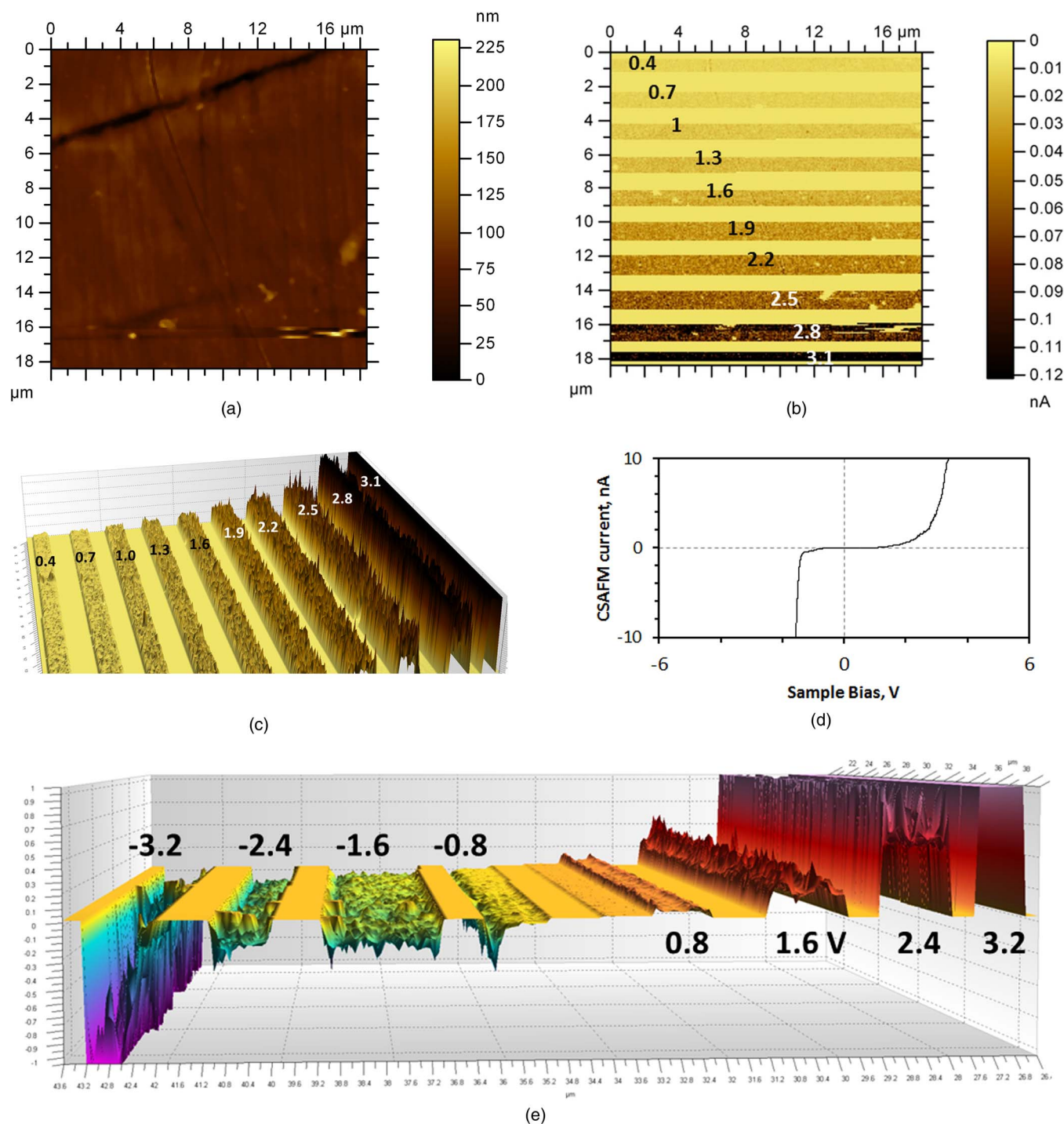
Figure 6. Current-sensing AFM images for samples emersed at 0 V. 6(a): Topography. 6(b): Current map. 6(c): Three-dimensional current map. 6(d): Current-voltage curve. 6(e): Same as 6(c) but including both positive and negative currents. See text for details.

topographical image, a current map, a current map in 3D and a current-voltage curve ($I − V$ curve, curve at right) as recorded by the CS-AFM probe are displayed. Similar measurements for type-III films were not successful, presumably due to these being thicker, more rough, and mechanically weaker (more "fluffy") than type-I films. Therefore, no results are presented for type-III films here.

For the current maps, the bias voltage was changed manually during imaging; a new value was entered approximately every 1 μm scanned.

For the sample emersed at 0 V in Fig. 6, the bias voltage was thus stepped intermittently between a "background bias" of 0.1 V and a "peak bias". The response is apparent in the current map as the bright (background bias) and darker (peak bias) areas. The peak bias was increased from 0.3 V to 3 V in units of 0.3 V per step. This resulted in larger and larger currents as the scan progressed, corresponding to darker and darker colors in the current map, Fig. 6. For Fig. 6e, peak bias was varied between negative biases of −3.2 V and positive bias of 3.2 V. Going to negative peak biases resulted in only small currents
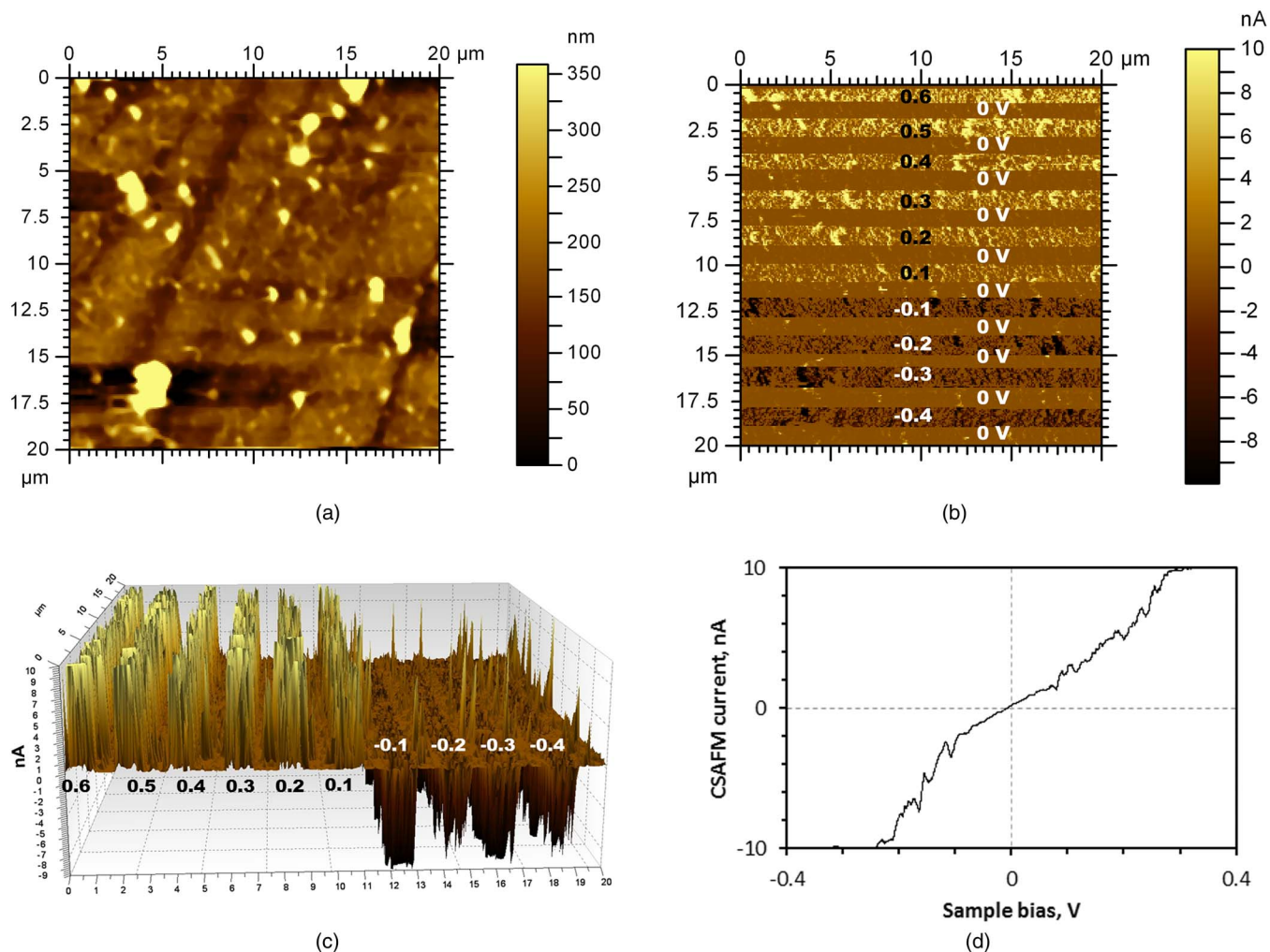
Figure 7. Current-sensing AFM images for samples emersed at 1.6 V. 7(a): Topography. 7(b): Current map. 7(c): Three-dimensional current map. 7(d): Current-voltage curve. See text for details.

which were independent on bias level. A breakdown and large currents were observed at −3.2 V.

For the sample emersed at 1.6 V the peak bias was increased from −0.5 V to 0.5 V in units of 0.1 V per step. The background bias was 0 V. In this case the brightest areas and the darkest areas correspond to current flow in opposite directions. The areas intermediate in color correspond to low or zero current (c.f. the adjacent color bar).

There is thus a very noticeable difference in current vs. bias ($I - V$) characteristics between the samples emersed at 0 V and 1.6 V. Those for the sample emersed at 1.6 V are quite symmetrical. For the latter the current changes sign in response to a change in sign of the bias, and the currents are similar in magnitude in both directions for a given absolute value of the bias. For those emersed at 0 V the current-voltage characteristics are those of a diode at positive bias and moderate values of negative bias, but with a steep onset of negative current at a certain negative bias.

The $I - V$ curves (Figures 6d and 7d) confirm the difference for the two samples seen in the current maps. The curves were reproducible for all points that were probed on the sample. At higher values of bias at either end of the scan, some higher deviations in the current values may be present, though. For the sample emersed at 0 V the curve has a zero-current region for bias from +3 V to approximately −0.75 V to −3 V. At negative bias the current becomes negative and decreases steeply with potential. This is believed to be due to breakdown of the film. On the positive-bias side the current increases less sharply in magnitude as the magnitude of the voltage gets larger, and the behavior

is clearly non-linear. For the sample emersed at 1.6 V the I-V curve is symmetrical, the middle portion approximating to a straight line.

The two samples employed for the CS-AFM measurements display similar surface topography except for some extra features apparent on the surface of the sample emersed at 1.6 V. These protrusions were also conducting, c.f. Fig. 7.

Discussion

The ex-situ CS-AFM measurements (current maps and I-V characteristics, Figs. 6 and 7) are consistent with the in-situ conductivity measurements, and display a significant increase in the current and change in shape of I-V curves when electrodes are emersed at potentials of 1.6 V compared to that for films emersed at 0 V. Likewise, the existence of Mott-Schottky behavior in-situ is consistent with the ex-situ current-voltage characteristics at low emersion potential, and correspond to those of a p-type semiconductor with a single space charge region (diode). At high emersion potential the current-voltage characteristics were approximately linear at all probe positions. The entire film appears ohmically conducting with no visible influence of semiconductor space charges on the current-voltage characteristics. The consistency between ex-situ (CS-AFM) and in-situ (Mott-Schottky measurements, coloration, conductivity) leads to the conclusion that the conductivity changes are not related to the presence of liquid electrolyte but an intrinsic property of the film.

The in-situ conductivity measurements reported above represent a direct observation of a significant increase in the conductivity in the potentials around B-peak, above 1.2 V vs. RHE in our electrochemically synthesized iridium oxide films, see Fig. 5. The CS-AFM results, the existence of a Mott-Schottky capacitance and the in-situ conductivity results therefore all rather directly demonstrate that the oxide layer goes through a semiconducting state in the reduced form to a state of metallic conductivity in the oxidized form, and the transition potential is at 1.2 V vs RHE. Therefore, we conclude that the conductivity of EIROF is directly affected by the applied potential.

The electrochemically deposited iridium oxide films (EIROF) appear to share many of the properties of anodically formed iridium oxide films (AIROF) such as anodic coloration, an identifiable flatband potential of similar magnitude, and similar voltammograms. It is therefore relevant to compare our EIROF results with the AIROF literature in the discussion below under the qualification that more subtle differences may exist between the two types of films.

In view of earlier work it is natural to associate the effect of the applied potential on conductivity and other properties with the intercalation reaction Eq. (1). In the rigid band approximation of Granqvist[3,4] the electron in Eq. (1) enters existing electronic levels in the oxide.[3] Since four out of the five states per formula unit in the t_{2g}-band[28–30] are filled in pure IrO_2, one extra electron per formula unit just fills the t_{2g}-band when the oxide is reduced according to Eq. (1). In other words, the intercalation process forces the Fermi level out of the t_{2g} band of the bulk oxide. This is consistent also with the UPS results of Kötz et al.[46] in which they demonstrate the crossing of the Fermi level into the bulk oxide upon oxidation. According to the explanation of Granqvist[3,4] for electrochromism in octahedrally coordinated oxides, color changes appear since the filling of bands (e.g. the Fermi level shifts out of the t_{2g} band referred to above) introduce new electronic transitions in the material and thus causes its color to change. The possible electronic transitions in the material in the reduced state are those across a (large) bandgap, whereas those in the oxidized state are (smaller) intraband transitions. This causes the oxide to change from transparent to blue. Since the conductivity changes observed here are easily accommodated within the same picture — band filling upon reduction and depletion upon oxidation — we conclude that the in-situ conductivity measurements comply with the balance of electronic properties of iridium oxide.

The characteristics of EIROF may thus be separated into three different regions. Below the flatband potential at 0.65 V (Fig. 5) the characteristics are those of a p-type semiconductor in depletion. In the potential region between the transition to high conductivity at 0.65 V and 1.2 V the oxide may be also be described as a semiconductor, but one in which an accumulation layer is present at the oxide-solution interface. This is in line with the proposals of Silva et al.[41] According to these authors the conductivity is associated with a crossing of the Fermi level and the valence band edge locally at the solid-solution interface, therefore leading to a surface-confined conductivity. However, our results show that any change in surface conductivity cannot be significant; if it was it should turn up as a current through the conductivity probe. More importantly, the results also show the presence of yet another region at higher potentials associated with a rather large increase in conductivity. It is in principle possible that the potential range 0.65 V through 1.2 V (corresponding to an electronic energy range of 0.65 eV through 1.2 eV) indicates the degree of band bending required for the Fermi level to cross the band edge. However, this is difficult to reconcile with the presumably rather high doping level of the material. We therefore conclude that the conductivity transition at 1.2 V may be associated with a bulk-like transition of the electronic structure of the oxide.

Thus, above 1.2 V the Fermi level is positioned inside the valence band. Any significant variations in the potential are confined to the interface region of the electrolyte, and the oxide behaves as a metal. Any changes in the applied potential will appear mainly across this region (electrode surface and Helmholtz layer). In this case, therefore, the entire electronic structure (band edges) will move up and down with the applied potential relative to any reference electrode in the electrolyte. In the parlance of semiconductor-electrochemistry the bands are "unpinned".[47] Below 1.2 V the Fermi level is inside bandgap, at least for the bulk; the electrode behaves as a semiconductor, and most of the applied potential is used to build the space charge layer of the electrode. In this case changes in the applied potential will be expected to appear across the space charge in the semiconductor. The bands are therefore "pinned".[47]

Having clarified the electronic structure of the oxide as a function of potential we now suggest that the transition of type I to type III film during film growth shown in Fig. 2 is an effect of the film thickness becoming more than one space-charge layer thick. The detailed explanation of this effect is given below and supported by the diagram in Fig. 8. The figure is organized in three rows according to film type: For each of the three types of film discussed above the figure shows the CV collected during growth with the cycle numbers included, a schematic highlighting how the different types of peaks change during film growth, and an associated band diagram at the potentials of the A-peak (below 1.2 V).

When the film is less than one space charge region thick, charge carriers are driven through the film by slight imbalances between strong electrical fields and large concentration gradients in the space charge region.[48] For a given driving force the transport of charges (protons and holes, Eq. (1)) inside the film is facilitated and will occur more swiftly than in the case where only solid state diffusion is operative.[41,49] In this case an increase in both A and B peak currents are observed during the electrochemical synthesis but no peak shifts. This process will proceed until the film is one space charge layer thick. In Fig. 8 this situation is described in the first row, and is what we have labeled type-I film above.

When the film becomes thicker than one space-charge region a diffusion region emerges in the (quasi-neutral) bulk of the film, which requires the applied potential to provide an additional driving force over that necessary for thin films to support a given intercalation rate. The diffusion region therefore tends to block the A-peak process at the potential at which it took place in the thin-film case, i.e. approximately 0.8 V. The peak current thus decreases without shifting on the potential axis. The film with partial or a completely blocked A-peak is presented in the second row of Fig. 8 and is labeled type-II to type-III. In the absence of a semiconducting-to-conducting transition in the oxide the same blocking would have been expected for the B-peak. However, close to the potential of the B-peak (1.2 V), the conductivity of the film is significantly increased. The applied potential now appears across the Helmholtz layer at the solid-solution interface instead of inside the oxide films (unpinning). This alters the difference in electrochemical potential of intercalation ions inside the film relative to those in the solution uncurtailed; the entire potential now goes into forcing these intercalation ions into or out of the film,[17,32] depending on scan direction. Some of the charge that from a purely thermodynamic perspective should have entered the film at the potential of the A-peak is thus transferred to the B-peak. In other words, some of the charge of the A-peak has been delayed so that it appears at the potentials of the B-peak.

In addition to the block-release effect for the A-peak, a potential shift of the B-peak in Fig. 2 is actually present after 50 cycles of film growth. This appears exactly at the number of cycles when the growing film becomes thicker than one space charge region. This confirms the suggestions above; the origin of the shift for the B-peak after 50 cycles may be taken to be the same block-release effect as for the A-peak and is thus also related to the conductivity transition.

In addition to the block-release effect suggested above, our growth voltammograms contain one more interesting feature: After the transition from type I to Type III film continued cycling in the precursor solution leads to a further increase of the A-peak. This is readily explained in terms of the discussion here: Areas on the electrode at which the film did not reach the critical thickness of one space-charge region will continue to grow as type-I films until such a critical thickness has been reached. One may consider these areas as type-I islands in the type-III film.
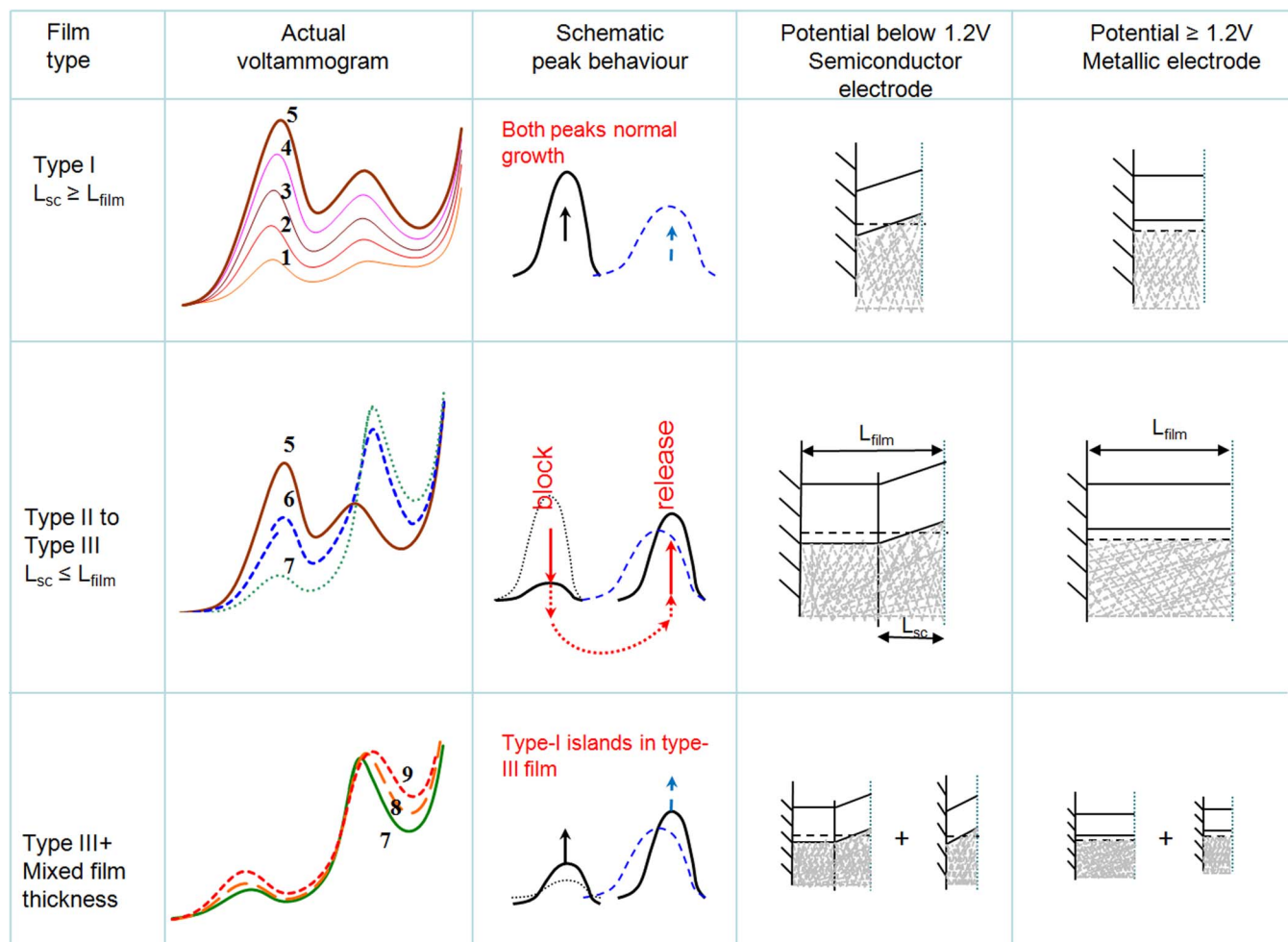
Figure 8. Explanation diagram for the block-release behavior of the voltammograms collected during growth of EIROF.

Gottesfeld et al.[50] discussed the shape of voltammograms of AIROF and other types of conductivity-switching films in terms of a simple power dependence of the film resistance on the oxidation state.[50] The model predicts among other things that for increasing sweep rate the voltammetric peaks will shift to more positive potentials,[50] p. 20]. This is the case in Figures 3 and 4. However, during film growth in Fig. 2 the A-peak appears at approximately the same potential for every cycle. For a purely resistive film with no space charges the resistance through the film would be proportional to film thickness for any given oxidation state. In such a case the A-peak would be shifted to higher and higher potentials as the film grows and becomes thicker.[50] This contradicts the experimental evidence, and the results cannot be analyzed solely in terms of the effects of film resistance. In our case it therefore becomes necessary to invoke the existence of both a space-charge region and a bulk region in addition to the conductivity change to explain the results.

We thus suggest here that the A-peak process in thick films is shifted to higher potentials than in thin films. This is due to transport limitations present in thick films, but absent or much less significant in thin. Charge is thus transferred from the A-peak to the B-peak in films significantly thicker than the thickness of one space-charge region. We note in passing that this also favors the proposition of a change in the bulk conductivity rather than the surface conductivity as it would be difficult to reconcile the block-release effect solely with a change in the surface conductivity.

This completed model is also consistent with explanation for aging effects in AIROF observed and explained by Bock and Birss.[1] They observed that voltammogramms for AIROFs changed from type I to type III after aging. The suggested explanation considered that A-peak process (the Ir(III)/Ir(IV) peak) was shifted to higher potentials because of longer pathways for charge transport associated with the partial delamination of the film upon aging. This is effectively equivalent to the mechanism suggested here.

Conclusions

Electrochemically synthesized iridium oxide (EIROF) behaves like a p-type semiconductor at low potentials, for which the flatband potential is similar to that of anodically formed iridium oxide (AIROF). The electronic and electrochemical properties of the EIROF change to those consistent with a bulk metallic electrode upon polarization of the electrode to potentials above 1.2 V vs. RHE.

In-situ conductivity and CS-AFM measurements show that the conductivity of the films increases at approximately 400 mV positive of the flatband potential. The conductivity changes are therefore due to changes in the bulk of the oxide with potential and not due to conductivity changes associated with the formation of an accumulation layer in the p-type oxide above the flatband potential. The results are thus consistent with a band model for the oxide in which the valence band is nearly filled with electrons upon proton insertion at low potentials. Oxidation of the film and the associated proton expulsion at high potentials shifts the Fermi level to within this band for the whole bulk.

These results also demonstrate the utility of in-situ conductivity measurements and ex-situ CS-AFM in the study of oxides displaying semiconductor-to-metal transitions.

The voltammetric behavior of the films during growth and aging can be rationalized in terms of the observed conductivity changes occurring in the film. The intercalation properties of thin films are dominated by the presence of space-charge layers extending across the entire film. Thicker films will contain a diffusion region in the bulk in addition to the space-charge region for which there will be no field-enhancement of transport rates. This leads to a block-release effect for voltammetric peaks during film growth and aging.

ORCID

Richard G. Haverkamp ⓘ https://orcid.org/0000-0002-3890-7105

References

1. C. Bock and V. I. Birss, *J. Electrochem. Soc.*, **146**, 1766 (1999).
2. S. Gottesfeld and J. D. E. McIntyre, *J. Electrochem. Soc.*, **126**, 742 (1979).
3. C. G. Granqvist, *Sol. Energy Mater. Sol. Cells*, **32**, 369 (1994).
4. C. G. Granqvist, *Thin Solid Films*, **564**, 1 (2014).
5. S. Gottesfeld and S. Srinivasan, *J. Electroanal. Chem.*, **86**, 89 (1978).
6. Ch. Comninellis and G. P. Vercesi, *J. Appl. Electrochem.*, **21**, 335 (1991).
7. L. Ouattara, S. Fierro, O. Frey, M. Koudelka, and C. Comninellis, *J. Appl. Electrochem.*, **39**, 1361 (2009).
8. S. Trasatti, *Interfacial Electrochemistry*, A. Wieckowski, Editor, p. 769, Marcel Dekker, New York (1999).
9. S. Trasatti, *Electrochimica Acta*, **36**, 225 (1991).
10. S. Trasatti, *Mater. Chem. Phys.*, **16**, 157 (1987).
11. S. Trasatti, *Electrochimica Acta*, **29**, 1503 (1984).
12. S. Trasatti, *J. Electroanal. Chem.*, **111**, 125 (1980).
13. R. G. Haverkamp, A. T. Marshall, and B. C. C. Cowie, *Surf. Interface Anal.*, **43**, 847 (2011).
14. A. Marshall, B. Børresen, G. Hagen, S. Sunde, M. Tsypkin, and R. Tunold, *Russ. J. Electrochem.*, **42**, 1134 (2006).
15. A. Marshall, S. Sunde, M. Tsypkin, and R. Tunold, *Int. J. Hydrogen Energy*, **32**, 2320 (2007).
16. R. Tunold, A. T. Marshall, E. Rasten, M. Tsypkin, L.-E. Owe, and S. Sunde, *ECS Transactions*, **25**, 103 (2010).
17. I. A. Lervik, M. Tsypkin, L.-E. Owe, and S. Sunde, *J. Electroanal. Chem.*, **645**, 135 (2010).
18. L.-E. Owe, I. A. Lervik, M. Tsypkin, M. V. Syre, and S. Sunde, *J. Electrochem. Soc.*, **157**, B1719 (2010).
19. S. Sunde, I. A. Lervik, M. Tsypkin, and L.-E. Owe, *Electrochimica Acta*, **55**, 7751 (2010).
20. P. Steegstra and E. Ahlberg, *J. Electroanal. Chem.*, **685**, 1 (2012).
21. V. I. Birss, C. Bock, and H. Elzanowska, *Can. J. Chem.*, **75**, 1687 (1997).
22. A. Ruban, B. Hammer, P. Stolze, H. L. Skriver, and J. K. Nørskov, *J. Mol. Catal. A: Chem.*, **115**, 421 (1997).
23. H. L. Xin, A. Vojvidic, J. Voss, J. K. Nørskov, and F. Abild-Pedersen, *Phys. Rev. B*, **89**, 115114 (2014).
24. J. Suntivich, K. J. May, H. A. Gasteiger, J. B. Goodenough, and Y. Shao-Horn, *Science*, **334**, 1383 (2011).
25. A. Vojvodic and J. K. Nørskov, *Science*, **334**, 1355 (2011).
26. S. A. Akhade and J. R. Kitchin, *J. Chem. Phys.*, **137**, 084703-1 (2012).
27. M. F. Yuen, I. Lauks, and W. C. Dautremont-Smith, *Solid State Ionics*, **11**, 19 (1983).
28. L. F. Mattheiss, *Phys. Rev. B*, **13**, 2433 (1976).
29. J. M. Honig, in *Electrodes of conductive metallic oxides*, S. Trasatti Editor, p. 1, Elsevier, Amsterdam (1980).
30. J. B. Goodenough, *Prog. Solid State Chem.*, **5**, 145 (1971).
31. S. H. Glarum and J. H. Marshall, *J. Electrochem. Soc.*, **127**, 1467 (1980).
32. S. Gottesfeld, *J. Electrochem. Soc.*, **127**, 1922 (1980).
33. J. Kukkonen, O. Fórsen, J. Aromaa, and S. Yläsari, *Mat. Sci. Forum*, **192–194**, 213 (1995).
34. S. A. M. Marzouk, *Anal. Chem.*, **75**, 1258 (2003).
35. J. Hu, M. Abdelsalam, P. Bartlett, R. Cole, Y. Sugawara, J. Baumberg, S. Mahajan, and G. Denuault, *J. Mater. Chem.*, **19**, 3855 (2009).
36. S. Sunde, R. Ødegård, and G. Hagen, *J. Electrochem. Soc.*, **138**, 2561 (1991).
37. M. S. Burke, L. J. Enman, A. S. Batchellor, S. Zou, and S. W. Boettcher, *Chem. Mater.*, **27**, 7549 (2015).
38. M. Burke Stevens, L. J. Enman, A. S. Batchellor, M. R. Cosby, A. E. Vise, C. D. M. Trang, and S. W. Boettcher, *Chem. Mater.*, **29**, 120 (2017).
39. Y. Zhao, E. A. Hernandez-Pagan, N. M. Vargas-Barbose, J. L. Dysart, and T. E. Mallouk, *J. Phys. Chem. Lett.*, **2**, 402 (2011).
40. E. N. El Sawy and V. I. Birss, *J. Mater. Chem.*, **19**, 8244 (2009).
41. T. M. Silva, A. M. P. Simoes, M. G. S. Ferreira, M. Walls, and M. D. Belo, *J. Electroanal. Chem.*, **441**, 5 (1998).
42. H. Elzanowska and V. I. Birss, *J. Appl. Electrochem.* **23**, 646 (1993).
43. P. G. Pickup and V. I. Birss, *J. Electrochem. Soc.*, **135**, 126 (1988).
44. L.-E. Owe, M. Tsypkin, and S. Sunde, *Electrochimica Acta*, **58**, 231 (2011).
45. P. G. Pickup and V. I. Birss, *J. Electroanal. Chem.*, **240**, 185 (1988).
46. E. R. Kötz and H. Neff, *Surf. Sci.*, **160**, 517 (1985).
47. R. Memming, *Semiconditor Electrochemistry*, Wiley-VCH, Weinheim (2001) p. 188
48. N. W. Ashcroft and D. N. Mermin, *Solid State Physics*, Saunders College Publishing, Philadelphia (1976) pp. 606–608
49. J. H. Kaufman, E. J. Mele, A. J. Heeger, R. Kaner, and A. G. MacDiarmid, *J. Electrochem. Soc.*, **130**, 571 (1983).
50. S. Gottesfeld, A. Redondo, I. Rubinstein, and S. W. Feldberg, *J. Electroanal. Chem.*, **265**, 15 (1989).